

Dynamic Assembly of Small Parts in Vortex–Vortex Traps Established within a Rotating Fluid

Taehoon Lee, Yaroslav I. Sobolev, Olgierd Cybulski, and Bartosz A. Grzybowski*

Stable, purely fluidic particle traps established by vortex flows induced within a rotating fluid are described. The traps can manipulate various types of small parts, dynamically assembling them into high-symmetry clusters, cages, interlocked architectures, jammed colloidal monoliths, or colloidal formations on gas bubbles. The strength and the shape of the trapping region can be controlled by the strengths of one or both vortices and/or by the system's global angular velocity. The system exhibits a range of interesting dynamical behaviors including a Hopf-bifurcation transition between equilibrium-point trapping and the so-called limit cycle in which the particles are confined to circular orbits. Theoretical considerations indicate that these vortex–vortex traps can be further miniaturized to manipulate objects with sizes down to $\approx 10 \mu\text{m}$.

The ability to trap and manipulate small objects in three dimensions—using either optical,^[1–3] magnetic,^[4,5] acoustic,^[6] or dielectrophoretic fields^[7] or microfluidic flows^[8,9]—has enabled applications ranging from atom-by-atom assembly,^[10] to Bose–Einstein condensation,^[11] to the manipulation of biomolecules,^[12,13] colloids^[14] and cells,^[15] to artificial insemination,^[16,17] and more.^[18,19] These methods differ in and are limited by the types and sizes of objects that can be manipulated—in particular, few can flexibly address and assemble larger nonmagnetic particles, from a tens of micrometers to millimeters, such as the components of mechanical systems or optical devices,^[20,21] or tissue-like assemblies.^[22,23] Here, we describe trapping in this regime of sizes enabled by vortex flows created within a rotating frame of reference. Although vortices and vortex systems^[24,25] typically do not create stable points within 3D flow fields, the situation changes when a pair of collinear vortices is generated within a fluid that is itself set on rigid-body rotation. Under these circumstances, the forces exerted by the vortices along the axis of rotation are accompanied by radially directed centripetal forces, in effect creating a region of strong

trapping. Using this arrangement, we demonstrate trapping and dynamic assembly of various particle clusters, cages, and interlocked architectures, as well as jammed colloidal monoliths or colloidal formations on gas bubbles. In these experiments, the shape of the trapping region—and, consequently, the morphology of the assembling structures—can be controlled by adjusting the strengths of one or both vortices and/or the system's global angular velocity, and can switch from a stable equilibrium point to a limit cycle via the so-called supercritical Hopf bifurcation. These findings illustrate how new modalities of dynamic self-assembly^[26]

and 3D manipulation become possible upon transition from static to noninertial, rotating frames of reference.

When a lighter particle of volume V and density ρ_p is immersed in a rotating fluid of density $\rho_L > \rho_p$, it experiences not only an upward-directed buoyant force $F_B = (\rho_p - \rho_L)Vg$, but also a centripetal force directed toward the axis of tube's rotation, $F_C(\mathbf{r}) = -(\rho_L - \rho_p)Vr\omega^2$, where ω is fluid's angular velocity and vector \mathbf{r} specifies particle's radial position (Figure 1a). In other words, the rotation of the tube imposes a confining harmonic potential, $E(r) = (\rho_L - \rho_p)Vr^2\omega^2/2$. As we have shown previously,^[27] for polymer beads inside tubes ≈ 1 cm in diameter, filled with various aqueous salt solutions and rotating at few thousand rpm, centrifugal acceleration is on the order of 10g (allowing us to neglect buoyancy effects in the subsequent discussion), and the beads localize along the fluid's axis of rotation. On the other hand, radially directed forces do not displace the beads along the tube's rotation axis and cannot, by themselves, create a stable trapping region in the axial direction.

To enable such lateral confinement, we designed a system (cf. Section S1, Supporting Information) in which two aluminum disks (radius 9.9 mm and thickness 16 mm) are fitted inside and near the two ends of the liquid-filled, rotating tube ≈ 1 cm in diameter. A permanent neodymium bar magnet (BX088-N52 from KJ Magnetics; $w = h = 12.5$ mm and $l = 25.4$ mm, magnetization along the w dimension = 588 mT) is placed at a distance d away from each disk (Figure 1b). The role of the magnets is to act as eddy-current brakes and slow down the rotation of the aluminum disks with respect to the rotation of the liquid-filled tube. Indeed, as the distance d between the disks and the magnets decreases, so does the disks' angular velocity, ω_1 . For a given d , ω_1 increases with but is always smaller than the angular velocity of the tube, ω (Figure 1c). This slowed-down rotation of the disks gives rise to

T. Lee, Dr. Y. I. Sobolev, Dr. O. Cybulski, Prof. B. A. Grzybowski
IBS Center for Soft and Living Matter
UNIST-gil 50, Eonyang-eup, Ulju-gun, Ulsan 689-798, Republic of Korea
E-mail: grzybor72@unist.ac.kr

T. Lee, Prof. B. A. Grzybowski
Department of Chemistry
UNIST

UNIST-gil 50, Eonyang-eup, Ulju-gun, Ulsan 689-798, Republic of Korea

 The ORCID identification number(s) for the author(s) of this article can be found under <https://doi.org/10.1002/adma.201902298>.

DOI: 10.1002/adma.201902298

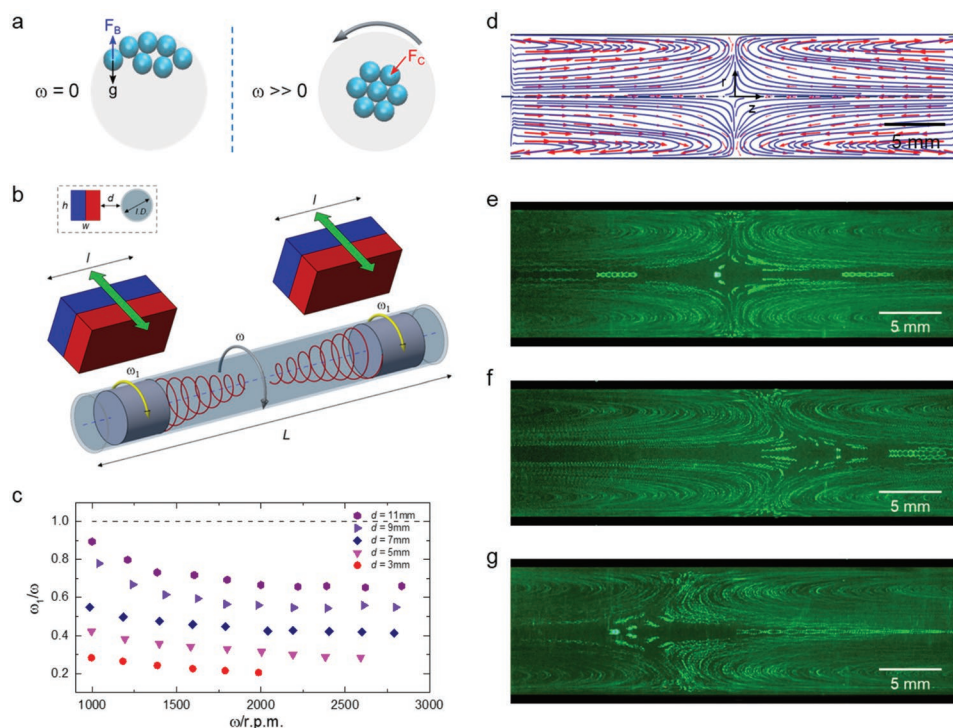


Figure 1. Experimental configuration of the vortex–vortex trapping system. a) Cross-sectional view of the tube housing lighter particles immersed in a denser liquid. When the tube rotates rapidly, the centripetal force, F_C , directed toward the axis of rotation dominates buoyant force, F_B . b) Scheme of the experimental arrangement in which two aluminum disks inside of the tube are slowed down by externally positioned permanent magnets (at variable distance d , see the inset), effectively creating vortex flows in the liquid. c) Rotational velocity of the disks, ω_1 , scales with but is smaller than that of the tube, ω . Different markers correspond to different distances, d , between the disks and magnets (see the legend). The data were measured for a mixture of water and glycerol (78:22, w/w; $\rho_L = 1.05 \text{ g cm}^{-3}$ and viscosity, 0.002 Pa s). Dashed line traces the $\omega_1/\omega = 1$ reference for which the disks are not retarded. d) Calculated velocity field of the flow and streamlines developed in the middle region of the tube. The calculations were performed in Comsol 5.1 for $d = 9 \text{ mm}$ and $\omega = 1500 \text{ rpm}$ with fluid's properties used in (c) and the same velocities of both disks, $\omega_1 \approx 925 \text{ rpm}$ e–g) Actual flow fields visualized by $10 \mu\text{m}$ fluorescent tracers in 25 wt% sucrose solution ($\rho_L = 1.11 \text{ g cm}^{-3}$). Panel (e) is for the case when both disks have similar angular velocities ($\omega_{1,\text{left}} \approx \omega_{1,\text{right}}$), and the vortices are symmetric. In panel (f), distance d is smaller for the left magnet–disk pair. Consequently, the left disk is slowed down more than the right one ($\omega_{1,\text{left}} < \omega_{1,\text{right}}$) and produces a stronger vortex reaching further to the right, beyond the mid-point of the tube. In panel (g), the opposite is true ($\omega_{1,\text{left}} > \omega_{1,\text{right}}$) and the right vortex is stronger.

vortex flows inside of the tube (Figure 1b,d–g). The calculated and experimental images of the flow field due to the vortices are illustrated in Figure 1d–g—as seen, the flow has lateral components directed from each disk toward the center of the tube, diverges near the tube's center, and returns toward the disks along the tube's walls. Importantly, because the outward flows near the mid-plane are opposed by the radially confining harmonic potential (cf. above), we expect that for appreciably high rotation rates of the tube (imposing radial confinement) and for strong enough vortex flows (establishing lateral confinement), the central region can trap particles lighter than the fluid. We note that in experiments with very small particles, it is sometimes beneficial to place additional, tightly fitting rings between the disks and the central region with particles (see Figure 2a)—this prevents the small particles from getting stuck in the gaps between the disks and the tube and jamming the former.

Examples in Figure 2 demonstrate that the system thus set up can act as a 3D fluidic trap. In Figure 2a, six spherical beads (diameter $D = 250 \mu\text{m}$; density, $\rho_p = 0.98 \text{ g cm}^{-3}$) are placed in a cylindrical glass tube (ID = 10 mm ; OD = 15 mm ; length, $L = 180 \text{ mm}$) filled with a mixture of water and glycerol (78:22, w/w; $\rho_L = 1.05 \text{ g cm}^{-3}$ and viscosity, 0.002 Pa s) and

rotating at $\omega = 2200 \text{ rpm}$. When the flanking magnets are far away and the difference in the angular velocity of the tube and the aluminum disks is not very pronounced (i.e., $\omega_1/\omega \gtrsim 0.9$), the assembly is dominated by radial/centripetal forces and the beads align along the axis of rotation. When, however, the magnets are placed closer to the disks ($d \approx 11\text{--}13 \text{ mm}$) and slow them down perceptibly, vortex flows emerge and localize the beads to the mid-point of the tube, where they arrange into an octahedral cluster. Figure 2b,c shows full phase diagrams quantifying organization of $n = 4$ and $n = 6$ particles for various values of ω and d . The diagrams share several similarities for both n 's. For instance, when d is small and the aluminum disks are markedly retarded, the strong vortices extend farther from the disks and give rise to swirling flows near mid-plane—consequently, the particles are not trapped to a stable, point-like region but exhibit orbiting trajectories in this plane (gray regions in the phase diagrams; also see discussion later in the text). In contrast, for large d (weak vortices) and large values of ω , the assemblies are dominated by centripetal forces and chain-up along the rotation axis. Trapping to a stable mid-point of the tube is observed for intermediate d and ω values—we note that for $n = 4$, only one type of a cluster (tetrahedral) is

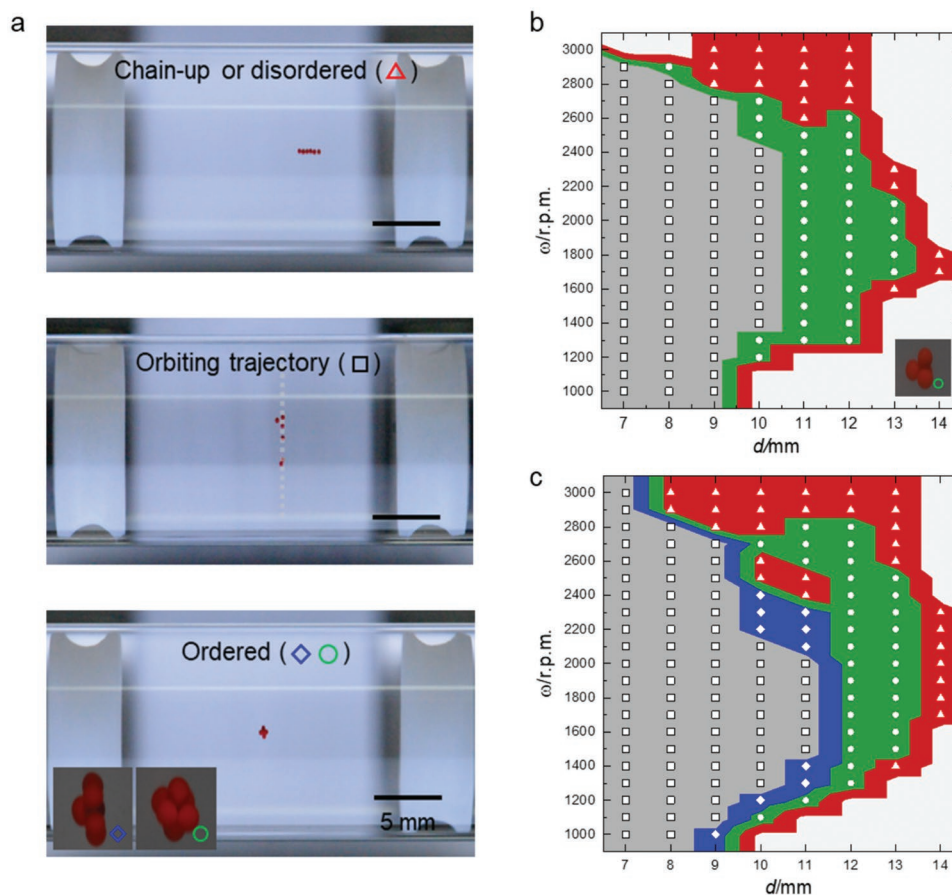


Figure 2. Trapping of particle clusters and phase diagrams. a) Three predominant modes of organization illustrated here for six $D = 250 \mu\text{m}$ particles: top) linear assembly along the axis of rotation; middle) particles orbiting along the tube's mid-plane; bottom) stable particle clusters in the trapping region (insets show two possible polymorphs). In the photographs, notice white, tightly fitting plastic rings inserted into the tube to prevent the small particles from jamming the aluminum disks (though, if disks are made to fit the tube relatively tightly, such disks are not necessary). Phase diagrams for systems of b) $n = 4$ and c) $n = 6$ of $250 \mu\text{m}$ particles. Phases are denoted by different markers corresponding to the images in (a). The markers indicate experimental results and the color map is drawn by interpolating the data. Unmarked/white regions represent cases where the particles' dynamics cannot be easily determined/classified (e.g., when the particles collide with the disks).

observed (green region in Figure 2b) but for $n = 6$, there are two polymorphs, octahedral and pentagonal-pyramid clusters (in Figure 2c, green and blue regions, respectively).

Polymorphs are also observed for some other particle numbers (e.g., $n = 5, 7, 9$, and 10 but not for highly symmetric $n = 8$; Figure 3a; Figure S7a, Supporting Information). Perhaps the most interesting case is for $n = 13$ which is relevant to the centuries-old mathematical problem of the kissing number—that is, how many hard spheres can surround and touch a common central sphere. Although the problem dates back to Newton, it was only in 1953 that it was formally proven that in 3D, the maximum kissing number is 12, with the possibility to arrange outer spheres in infinitely many configurations.^[28,29] Our experimental system not only realizes several such configurations but, by changing particle densities, allows for the selection of the most dominant polymorph. For instance, for all identical spheres (e.g., in Figure 3b, $D = 500 \mu\text{m}$, $\rho_p = 1.13 \text{ g cm}^{-3}$, $\rho_L = 1.15 \text{ g cm}^{-3}$, $\omega = 750\text{--}1250 \text{ rpm}$, $d = 6\text{--}8 \text{ mm}$), the fcc-packed structure is most frequently observed and remains stable over a relatively wide range of parameters ($\Delta d \approx 1.5 \text{ mm}$). An icosahedral packing is less frequent and less stable (only

within $\Delta d \leq 0.3 \text{ mm}$) and so is the modified icosahedral packing in which the two five-sphere rings surrounding the three (core) spheres are slightly further apart. Interestingly, despite this small difference, the icosahedral and icosahedral-like structures are readily distinguishable because they are differently oriented with respect to the rotation axis (since the harmonic confining potential strives to minimize the cluster's moment of inertia with respect to the tube's axis of rotation; Figure 3c). Now, when one blue particle is replaced by a lighter ($\rho_p = 0.98 \text{ g cm}^{-3}$) red sphere of the same size, this sphere—experiencing largest confining force—localizes preferentially to the cluster's center and the icosahedral packing becomes dominant (Figure 3d), with the other two being observed only sporadically. When three lighter spheres are used, they align along the axis of tube's rotation, completely eliminating formation of the fcc structure (Figure 3e).

A rich variety of trapped structures can be observed with components having different sizes and/or nonspherical shapes. For instance, smaller spheres can form centrally positioned rings around larger spheres (Figure 4a) or bubbles (Figure 4b). Polygonal plates can be assembled into boxes around spherical

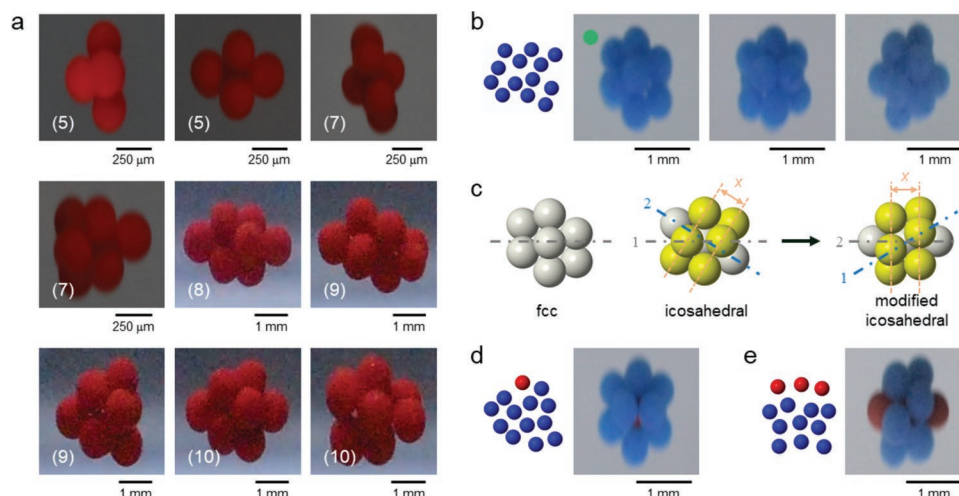


Figure 3. Examples of polymorphic particle clusters. a) Clusters formed by $n = 5$ – 10 particles (numbers of particles are in the parentheses). Polymorphs are not observed only for $n = 8$. For $n = 5$ and 7 , the sizes of particles are $250 \mu\text{m}$ ($\rho_p = 0.98 \text{ g cm}^{-3}$) and the solution is a mixture of water and glycerol ($\rho_L = 1.05 \text{ g cm}^{-3}$). The ordered clusters were obtained at $\omega = 1500$ – 2500 rpm and $d = 10$ – 13 mm . For $n = 8$ – 10 , we used 1 mm particles ($\rho_p = 0.98 \text{ g cm}^{-3}$) and CsBr solution ($\rho_L = 1.2 \text{ g cm}^{-3}$) and obtained those clusters at $\omega = 3500$ – 4500 rpm and $d = 2$ – 4 mm . b) Polymorphs formed by $n = 13$ identical $D = 500 \mu\text{m}$ spheres. The structures are fcc, icosahedral, and modified icosahedral packings (from left to right). Green marker indicates dominant packing. c) Schematics of the three distinct packings. For each packing, the principal axis is indicated by a gray dash-dot line. The icosahedral and modified icosahedral packings (which look very similar but differ in the distance x between the outer rings of yellow-colored particles) can be distinguished by the rotation axis; “1” for the former and “2” for the latter. Experimental images of packings observed for systems consisting of d) 1 red and 12 blue spheres, and e) 3 red and 10 blue spheres. The red spheres ($\rho_p = 0.98 \text{ g cm}^{-3}$) are lighter than the blue ones ($\rho_p = 1.13 \text{ g cm}^{-3}$) and preferentially localize onto the axis of rotation. For 13-sphere packings, we used a mixture of 4.1 M NaCl solution and glycerol ($8/2, v/v; \rho_L = 1.15 \text{ g cm}^{-3}$).

particles (Figure 4c,d), whereas rings can be threaded onto rods (Figure 4e). In these experiments, the fidelity of assembly into perfectly ordered structures decreases with the number of the same-type particles present (as expected for glass-forming systems), and is also problematic with plate-like parts that tend to stack-up (e.g., in the box structures around spheres whereby, in the majority of cases, not all faces are “closed;” see Figure 4c,d and Figure S7 in the Supporting Information). Another interesting situation arises when large numbers of small particles are present such that they can fill the trapping region assuming its changing shape. Under these circumstances, the varying degrees of confinement can control particles’ jamming. For example, in Figure 5a, the collection of $D = 50 \mu\text{m}$, $\rho_p = 0.98 \text{ g cm}^{-3}$ particles is subject to only moderate radial confinement ($\omega = 800 \text{ rpm}$) and when the lateral, confining vortex flows become stronger—upon decreasing the distance to the magnets, d , from 20 to 9 mm—the agglomerate gradually evolves from an oblong ellipsoid to a roughly spherical formation. In contrast, when the vortices act on particles subject to stronger radial confinement, $\omega = 1800 \text{ rpm}$, they are jamming and cannot relax to the spherical shape. Instead, the formation changes from a dumbbell to a cylindrical shape (Figure 5b). Finally, we note that in these and other experiments we described, the trap can be made laterally asymmetric by using unequal distances of the magnets to proximal aluminum disks, thus individually adjusting vortex strengths. For instance, Figure 5c shows a half-ellipsoid assembly of $50 \mu\text{m}$ particles observed when the confining vortex acting from one direction is much stronger than that acting from the other (distances to the magnets $d_{\text{left}} = 8 \text{ mm}$ vs $d_{\text{right}} = 12 \text{ mm}$). Another example of an asymmetric shape is shown in Figure 5d illustrating time evolution and relaxation with time.

The properties of our vortex–vortex traps merit additional theoretical discussion. In general, the ability to trap particles derives from an interplay between centripetal forces, $\mathbf{F}_C = -(\rho_L - \rho_p)V\mathbf{r}\omega^2$ and the forces imparted on the particles by the vortices. A simplified yet realistic model—capturing most of trap’s characteristics—considers the drag forces the particles experience in vortex flows, $\mathbf{F}_{\text{vort}} = 3\pi\eta D\mathbf{u}$ where η is viscosity of the fluid, D is particle’s diameter, and \mathbf{u} is fluid’s velocity calculated numerically (ref. [30] and Figure 1d) for an axisymmetric geometry and with boundary conditions at the surfaces of the slowed-down disks obtained from their experimentally measured angular velocities (see Figure 1c). With these assumptions, we consider the radial, r , and axial, z , components of $\mathbf{F}_C(\mathbf{r}) + \mathbf{F}_{\text{vort}}$ to delineate the regions of trap’s stability for a particle of certain diameter. Maps in Figure 6a are (r, z) cross-sections near the rotating tube’s center ($-5 \text{ mm} < r < 5 \text{ mm}$, $-2 \text{ mm} < z < 2 \text{ mm}$) for $D = 100 \mu\text{m}$ particles ($\rho_p = 0.98 \text{ g cm}^{-3}$, $\rho_L = 1.05 \text{ g cm}^{-3}$, $\eta = 0.002 \text{ Pa s}$, and $\omega = 2000 \text{ rpm}$) and vortex strength decreasing from left to right (d increasing from 3 to 11 mm). A particle is only attracted into regions where $|\mathbf{F}| = 0$, and $\frac{\partial F_z}{\partial z} < 0$ and $\frac{\partial F_r}{\partial r} < 0$. Since pinpointing locations where $|\mathbf{F}| = 0$ is complicated by finite precision of numerically calculated flow fields, we highlight contours (white) where $|\mathbf{F}|$ is equal to some small value (say, 0.1 nN) such that the zero-force, equilibrium point is contained somewhere within the contour. Blue color indicates regions over which $\frac{\partial F_z}{\partial z} < 0$ and $\frac{\partial F_r}{\partial r} < 0$, which makes zero-force points there stable (if any); green color delineates regions where $\frac{\partial F_z}{\partial z} > 0$ or $\frac{\partial F_r}{\partial r} > 0$, so even zero-force point in these regions would be unstable. At $d = 3 \text{ mm}$, the on-axis zero-force point is unstable ($\frac{\partial F_r}{\partial r} > 0$), and

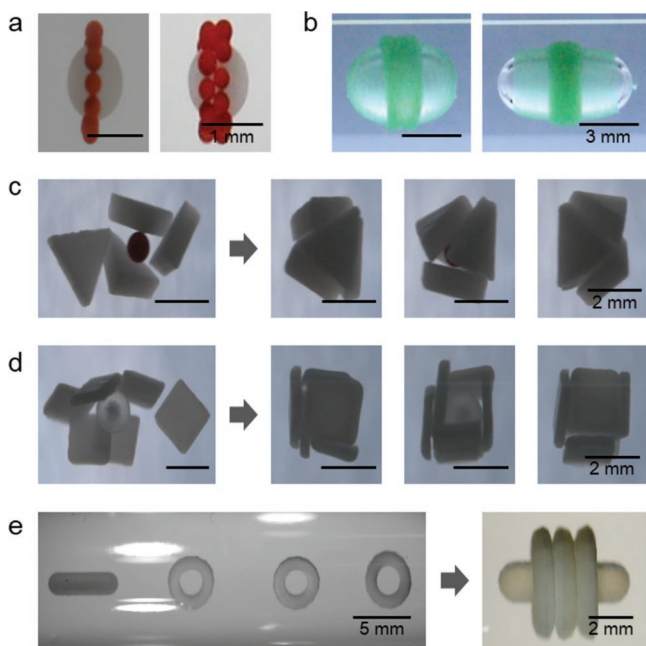


Figure 4. Examples of trapped structures assembled from nonidentical components. a) Binary structures with a single chain of 13 spheres (left) and double chain of 25 spheres (right) surrounding one large sphere. The diameters of spheres are 250 μm for the red ones ($\rho_p = 0.98 \text{ g cm}^{-3}$) and 1 mm for the white one ($\rho_p = 0.96 \text{ g cm}^{-3}$). Here, mixtures of water/glycerol (78/22, w/w; $\rho_L = 1.05 \text{ g cm}^{-3}$) and 2 M NaCl/glycerol (8/2, v/v; $\rho_L = 1.1 \text{ g cm}^{-3}$) were used for single- and double-chain structures, respectively. b) Colloids on air bubbles. 50 μm particles form a band around a centrally positioned air bubble in a solution of water/EG (5/5, v/v; $\rho_L = 1.06 \text{ g cm}^{-3}$). As the radial confining force increases from $\omega = 2000 \text{ rpm}$ (left) to 3000 rpm (right), the particles are more concentrated in the band and the bubble becomes more elliptical. Self-assembly of c) tetrahedral and d) cubic “cages.” In (c), four triangular plates (edge length, $a = 2 \text{ mm}$; $\rho_p = 1.02 \text{ g cm}^{-3}$) assemble into a “box” surrounding a central, $D = 800 \mu\text{m}$ sphere ($\rho_p = 0.98 \text{ g cm}^{-3}$). In the box in (d), two square plates ($a = 1.88 \text{ mm}$, $\rho_p = 1.02 \text{ g cm}^{-3}$) are stacked so the box has one face open, exposing the inner, $D = 1.6 \text{ mm}$ sphere ($\rho_p = 0.9 \text{ g cm}^{-3}$). e) An interlocked, “rotaxane” structure assembled from one rod ($D = 1.5 \text{ mm}$, $L = 6 \text{ mm}$, $\rho_p = 1.02 \text{ g cm}^{-3}$) and three rings ($D_{\text{inner}} = 2 \text{ mm}$, $D_{\text{outer}} = 4 \text{ mm}$, $\rho_p = 1.02 \text{ g cm}^{-3}$). The initial configuration of the components is essential for the formation of this assembly; the rod should not be placed between the rings or else disordered structures form, see also Figure S7d (Supporting Information). In (c)–(e), the plates, cylinders, and rings were fabricated via 3D printing and the solution was a mixture of fluorinated liquid (3M Novec 7200 Engineered Fluid) and silicone oil (PDMS, viscosity 10 cSt, Sigma Aldrich) in a 7/3 v/v ratio and density, $\approx 1.3 \text{ g cm}^{-3}$.

the only stable zero-force points are off the axis. Given that the model is axisymmetric, these two points correspond to a ring trajectory along the mid-plane of the tube—indeed, for strong lateral confinement, we see such trajectories in experiment (cf. Figure 2a–c and gray regions in the phase maps therein). For $d \geq 5 \text{ mm}$, the stable equilibrium point localizes onto the axis of rotation enabling trapping and assembly of 3D structures. As seen, when d increases, the shape of the trap changes from an oblate spheroid ($F_z > F_r$), to a sphere ($F_z \approx F_r$), to a prolate spheroid ($F_z < F_r$), which is again in agreement with our experimental observations (cf. Figure 5a). These characteristics of the trap are summarized in Figure 6b in which the pink

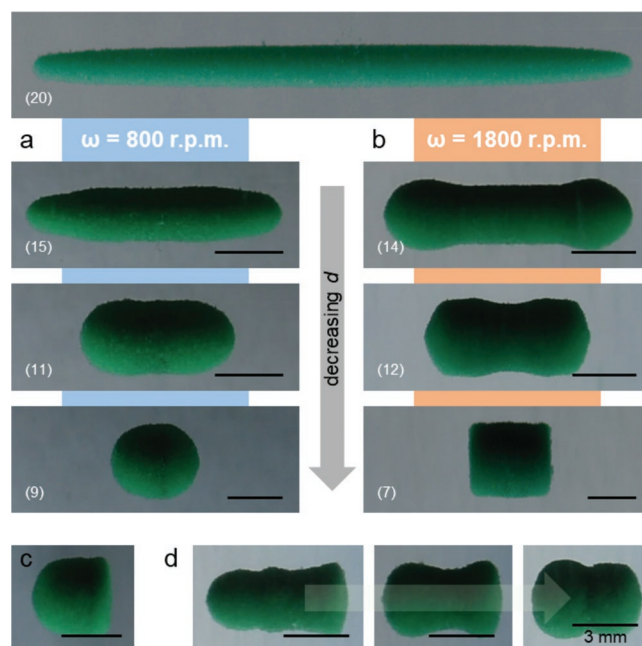


Figure 5. Particle's jamming and asymmetric assemblies. a) Gradual transformation—from an oblong ellipsoid to approximately a sphere—of a formation of large numbers of small particles. The top panel shows a structure at large d ($=20 \text{ mm}$) from which we studied morphological changes by sequentially decreasing d . Specific values of d in mm are given by white-font numbers in parentheses. b) “Jammed” transformation at increased radial confinement. In contrast to (a), stronger radial confinement prevents the assembly from relaxing to the spherical shape, instead, the monolith evolves from a dumbbell to a cylinder. The experiment is for 1800 rpm, but the effects of confinement become manifest already at 1200 rpm. c) Asymmetric assembly driven by disks rotating at different rates and creating vortices of different strengths. In this example, $\omega_{\text{tube}} = 1500 \text{ rpm}$ and $\omega_{1,\text{left}} < \omega_{1,\text{right}}$. d) Time evolution of an asymmetric colloidal assembly ($\omega_{\text{tube}} = 1400 \text{ rpm}$ and $\omega_{1,\text{left}} < \omega_{1,\text{right}}$). The arrow indicates passage of time, spanning a period of about an hour. In all experiments, the particles were 50 μm in diameter, had a density of 0.98 g cm^{-3} , and the solution was a mixture of fluorinated liquid (3M Novec 7200 Engineered Fluid) and silicone oil (PDMS, viscosity 10 cSt, Sigma Aldrich) in a 3/7 v/v ratio and density $\approx 1.08 \text{ g cm}^{-3}$. All scale bars are 3 mm.

contour traces the region of parameter space for which the trap is approximately isotropic (spherical).

We note that the transition between particle's ring orbit (“limit cycle”) and a stable trapping point (“stable equilibrium”) upon the change in single parameter d proceeds without hysteresis (cf. Figure S6, Supporting Information) and is a manifestation of the so-called supercritical Hopf bifurcation well known in the mathematical theory of dynamical systems.^[31] This is corroborated by Figure 6c–e plotting the centripetal force (directed toward the axis of rotation) and the drag force (directed away from this axis) at the mid-plane of the rotating tube for three different values of d and with other parameters held constant ($D = 100 \mu\text{m}$, $\omega = 1800 \text{ rpm}$, $\rho_L - \rho_p = 0.06 \text{ g cm}^{-3}$, $\eta = 0.002 \text{ Pa s}$); the stable points are marked by red circles. Interestingly, the model predicts not only the Hopf bifurcation but also the existence of two limit cycles for intermediate values of d (Figure 6d,f). We actually verified this prediction experimentally for the system of polystyrene particles ($D = 100 \mu\text{m}$, $\rho_p = 1.05 \text{ g cm}^{-3}$) in 25 wt% sucrose solution ($\rho_L = 1.11 \text{ g cm}^{-3}$)

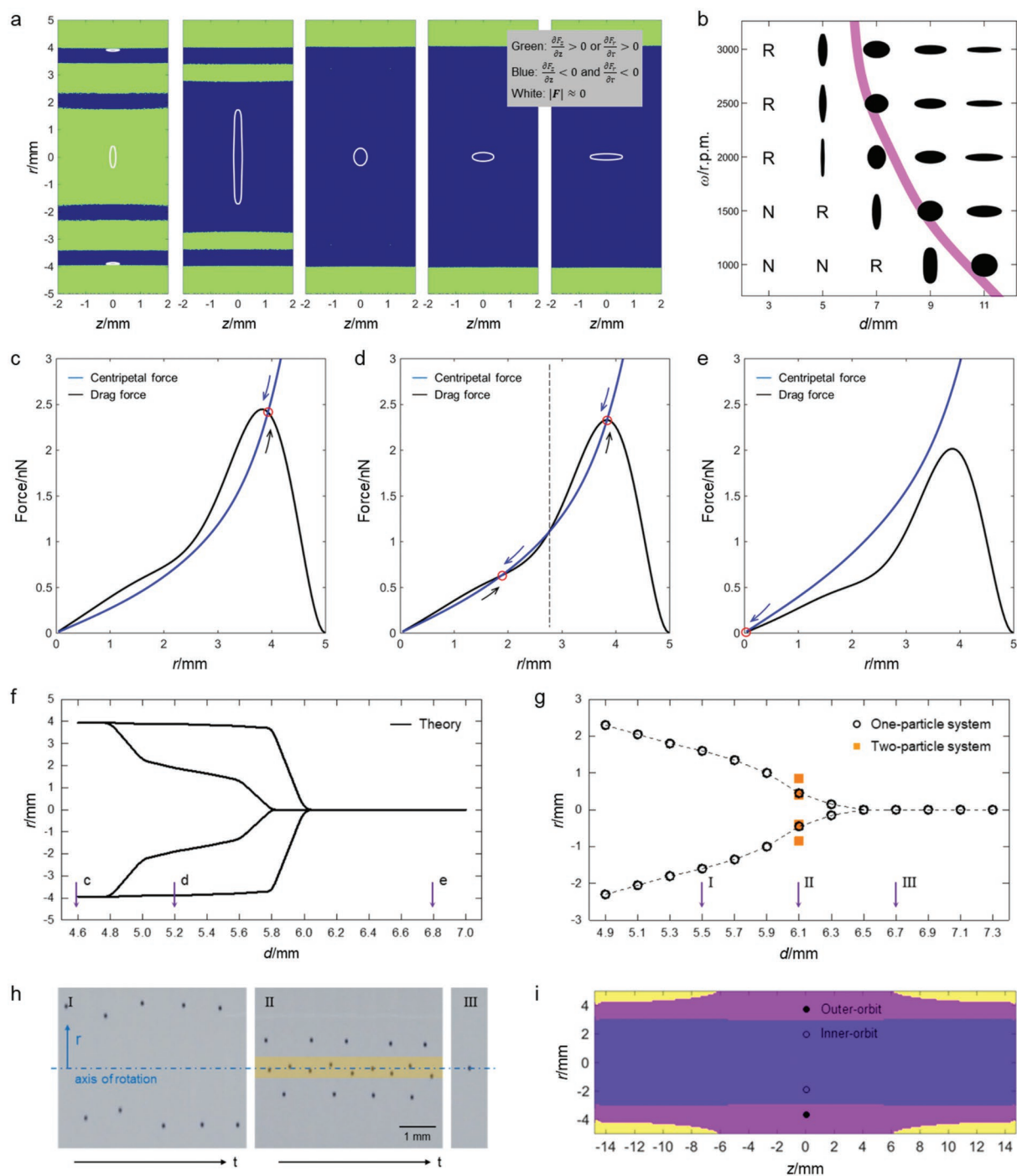


Figure 6. Theoretical studies of the vortex–vortex trap and Hopf bifurcation. a) Partial derivatives of force field (color map) and near-zero-force lines (white) for 100 μm particle system at $\omega = 2000$ rpm and $d = 3, 5, 7, 9,$ and 11 mm (from left to right). b) Various contours of the trapping region for 100 μm particle as a function of ω and d . Here, letter N denotes no-particle-trapping and R indicates a ring trajectory in the mid-plane of the tube. Regions for an isotropic shape of the trap (pink) were estimated by interpolating the simulation results. Confining force curves for states of c) a limit cycle ($d = 4.6$ mm), d) two limit cycles ($d = 5.2$ mm), and e) a stable equilibrium ($d = 6.8$ mm) at the mid-plane of the tube ($z = 0$) and plotted along the radial coordinate, r . The red circles indicate stable equilibrium positions of a particle at given conditions. The arrows and the dotted line are inserted to illustrate particle trapping. Stability maps of 100 μm particle system obtained from f) theoretical model and g) experiment. Theoretical model predicts the existence of two limit cycles at $4.8 < d < 6.0$. In the experiment, two limit cycles were observed only in a system of two particles; these two limit cycles converged into one limit cycle with a small change of distance, d ($\Delta d = 0.2$ mm). In (f) and (g), the arrows indicate the values of d at which data are used for (c)–(e) and (h). h) Experimental images for states of a limit cycle (I, $d = 5.5$ mm), two limit cycles (II, $d = 6.1$ mm), and a stable equilibrium (III, $d = 6.7$ mm). Colored region in the middle image (II) marks a smaller limit cycle. i) Basin of attraction for the two limit cycles. Basins of attraction for inner and outer orbits are distinguished by different colors. Here, the condition for calculation corresponds to that of (d). In (c)–(i), the rotational rate of the tube is 1800 rpm.

rotating at $\omega = 1800$ rpm and $d = 4.9\text{--}7.3$ mm (Figure 6g,h). When just one particle was used, it always located to one, inner orbit. However, with two particles present and $d \approx 6.1$ mm, the second particle occupied the larger-radius, outer orbit as illustrated in experimental images in Figure 6h. The relatively narrow range of parameters for which two orbits are occupied can be reasonably attributed to the fact that the inner-orbit limit cycle has a larger basin of attraction than the outer-orbit one (Figure 6i).

Finally, we note that a theoretical model described in Section S2 in the Supporting Information indicates that the lower limit for the size of a particle that can be trapped scales as $R^2 \approx \frac{C}{\omega^2} \left(\frac{(\omega - \omega_1)}{\omega} + 3 \frac{(\omega - \omega_1)^2}{\omega^2} \right)$, where $C = \frac{9K\eta^2}{4(\rho_L - \rho_P)\rho_L H^2}$, in which H is the distance between the aluminum disks and K is the dimensionless factor that depends on the ratio of H and the tube's inner diameter. Using this model, we estimate that at higher rotational rates (not available in our current setup for technical and safety reasons), the traps can be effective for particles with sizes down to ≈ 10 μm . For example, for $\omega = 10\,000$ rpm, $\omega_1 = 400$ rpm, $\eta = 2.175$ mPa s, $\rho_L = 1.104$ g cm $^{-3}$, $\rho_P = 0.98$ g cm $^{-3}$, ID = 10 mm, $H = 30$ mm, one should be able to trap particles of ≈ 6 μm radii.

In summary, we showed that by embedding vortex flows inside a rotating frame of reference, it is possible to realize purely fluidic 3D traps. Although theory suggests these traps can be further miniaturized and can potentially address single cells or colloids, the current experimental setup is limited to larger particles (>tens of micrometers), which is the size regime relevant to the manipulation and assembly of small-part mechanical systems and also of certain biological specimens, such as cell spheroids^[32] important in cell biology (and potentially benefitting from "clean," substrate-free positioning subject to spatially variable forces our system readily offers). We envision that for the assembly of small parts, it will be important to solidify the dynamic structures that form in the trap, perhaps by using liquid-solder methods.^[33,34] Last but not least, the traps exhibit a range of interesting nonlinear behaviors, including bifurcations, suggesting they can be used as test-beds for studying various dynamical systems comprised of different sized and/or shaped particles.

Supporting Information

Supporting Information is available from the Wiley Online Library or from the author.

Acknowledgements

The authors gratefully acknowledge generous support from the Institute for Basic Science Korea, Project Code IBS-R020-D1. T.L. performed most experiments. T.L. and Y.S. developed theoretical models. O.C. designed the aluminum-brake system and helped with experiments. B.A.G. conceived the project and supervised research. All authors participated in the writing of the manuscript.

Conflict of Interest

The authors declare no conflict of interest.

Keywords

3D confinement, dynamic self-assembly, Hopf bifurcation, particle trapping, vortex flows

Received: April 10, 2019

Revised: May 1, 2019

Published online: July 1, 2019

- [1] A. Ashkin, *Phys. Rev. Lett.* **1970**, 24, 156.
- [2] A. Ashkin, J. M. Dziedzic, *Science* **1987**, 235, 1517.
- [3] E. L. Raab, M. Prentiss, A. Cable, S. Chu, D. E. Pritchard, *Phys. Rev. Lett.* **1987**, 59, 2631.
- [4] T. R. Strick, J.-F. Allemand, D. Bensimon, A. Bensimon, V. Croquette, *Science* **1996**, 271, 1835.
- [5] J. V. Timonen, B. A. Grzybowski, *Adv. Mater.* **2017**, 29, 1603516.
- [6] A. Marzo, S. A. Seah, B. W. Drinkwater, D. R. Sahoo, B. Long, S. Subramanian, *Nat. Commun.* **2015**, 6, 8661.
- [7] C. Zhang, K. Khoshmanesh, A. Mitchell, K. Kalantar-zadeh, *Anal. Bioanal. Chem.* **2010**, 396, 401.
- [8] N. Sundararajan, M. S. Pio, L. P. Lee, A. A. Berlin, *J. Microelectromech. Syst.* **2004**, 13, 559.
- [9] A. Karimi, S. Yazdi, A. M. Ardekani, *Biomicrofluidics* **2013**, 7, 021501.
- [10] D. Barredo, V. Lienhard, S. de Léséleuc, T. Lahaye, A. Browaeys, *Nature* **2018**, 561, 79.
- [11] M. H. Anderson, J. R. Ensher, M. R. Matthews, C. E. Wieman, E. A. Cornell, *Science* **1995**, 269, 198.
- [12] M. D. Wang, H. Yin, R. Landick, J. Gelles, S. M. Block, *Biophys. J.* **1997**, 72, 1335.
- [13] A. H. B. de Vries, B. E. Krenn, R. van Driel, V. Subramaniam, J. S. Kanger, *Nano Lett.* **2007**, 7, 1424.
- [14] T. Li, S. Kheifets, D. Medellin, M. G. Raizen, *Science* **2010**, 328, 1673.
- [15] L. Lin, X. Peng, X. Wei, Z. Mao, C. Xie, Y. Zheng, *ACS Nano* **2017**, 11, 3147.
- [16] J. M. Nascimento, L. Z. Shi, S. Meyers, P. Gagneux, N. M. Loskutoff, E. L. Botvinick, M. W. Berns, *J. R. Soc., Interface* **2008**, 5, 297.
- [17] N. Hyun, C. Chandsawangbhuwana, Q. Zhu, L. Z. Shi, C. Yang-Wong, M. W. Berns, *J. Biomed. Opt.* **2012**, 17, 025005.
- [18] A. Jamshidi, P. J. Pauzauskie, P. J. Schuck, A. T. Ohta, P.-Y. Chiou, J. Chou, P. Yang, M. C. Wu, *Nat. Photonics* **2008**, 2, 86.
- [19] M. S. Friddin, G. Bolognesi, Y. Elani, N. J. Brooks, R. V. Law, J. M. Seddon, M. A. A. Neil, O. Ces, *Soft Matter* **2016**, 12, 7731.
- [20] A. B. Subramaniam, D. Yang, H.-D. Yu, A. Nemiroski, S. Tricard, A. K. Ellerbee, S. Soh, G. M. Whitesides, *Proc. Natl. Acad. Sci. USA* **2014**, 111, 12980.
- [21] K. A. Mirica, F. Ilievski, A. K. Ellerbee, S. S. Shevkoplyas, G. M. Whitesides, *Adv. Mater.* **2011**, 23, 4134.
- [22] V. A. Parfenov, E. V. Koudan, F. A. Bulanova, P. A. Karalkin, F. D. A. S. Pereira, N. E. Norkin, A. D. Knyazeva, A. A. Gryadunova, O. F. Petrov, M. M. Vasiliev, M. I. Myasnikov, V. P. Chernikov, V. A. Kasyanov, A. Y. Marchenkov, K. Brakke, Y. D. Khesuani, U. Demirci, V. A. Mironov, *Biofabrication* **2018**, 10, 034104.
- [23] J. V. I. Timonen, C. Raimondo, D. Pilans, P. P. Pillai, B. A. Grzybowski, *Nanoscale Horiz.* **2017**, 2, 50.
- [24] B. A. Grzybowski, H. A. Stone, G. M. Whitesides, *Nature* **2000**, 405, 1033.
- [25] B. A. Grzybowski, G. M. Whitesides, *J. Phys. Chem. B* **2002**, 106, 1188.

- [26] B. A. Grzybowski, K. Fitzner, J. Paczesny, S. Granick, *Chem. Soc. Rev.* **2017**, 46, 5647.
- [27] T. Lee, K. Gizynski, B. A. Grzybowski, *Adv. Mater.* **2017**, 29, 1704274.
- [28] G. G. Szpiro, *Kepler's Conjecture*, Wiley, Hoboken, NJ **2003**.
- [29] J. H. Conway, N. J. A. Sloane, *Sphere Packings, Lattices, and Groups*, Springer, New York **1999**.
- [30] COMSOL Multiphysics 5.1, COMSOL, Inc., Burlington, MA **2015**.
- [31] S. Strogatz, *Nonlinear Dynamics and Chaos*, CRC Press, Boca Raton, FL **2015**.
- [32] F. Pampaloni, E. G. Reynaud, E. H. K. Stelzer, *Nat. Rev. Mol. Cell Biol.* **2007**, 8, 839.
- [33] D. H. Gracias, J. Tien, T. L. Breen, C. Hsu, G. M. Whitesides, *Science* **2000**, 289, 1170.
- [34] T. G. Leong, P. A. Lester, T. L. Koh, E. K. Call, D. H. Gracias, *Langmuir* **2007**, 23, 8747.